Supplementary Information (SI) for Nanoscale Horizons.
This journal is © The Royal Society of Chemistry 2024

Cluster-doping in silicon nanocrystals

Atta ul Haq[1], Marius Buerkle[2], Bruno Alessi[2], Vladimir Svrcek[2], Paul Maguire[1], Davide Mariotti[1*]

[*] *davide.mariotti@strath.ac.uk*

[1] School of Engineering, Ulster University, York Street, Belfast BT15 1ED

[2] Renewable Energy Research Center, National Institute of Advanced Industrial Science and Technology (AIST), Tsukuba, Ibaraki, 305-8568, Japan

[3] Department of Design, Manufacturing & Engineering Management, University of Strathclyde, Glasgow, UK

SI-A. Additional transmission electron microscopy analysis

Detailed lattice fringes and line profiles have been presented in figures S1 to S3. Figure S1 reports line profile analysis of HR-TEM images of three NCs corresponding to the samples with NCs with mean diameter of 1.4 nm. The line profile analysis yields an average lattice spacing of 0.328 nm (111), 0.316 nm (111) and 0.318 nm (111) for NC-1, NC-2 and NC-3 respectively.

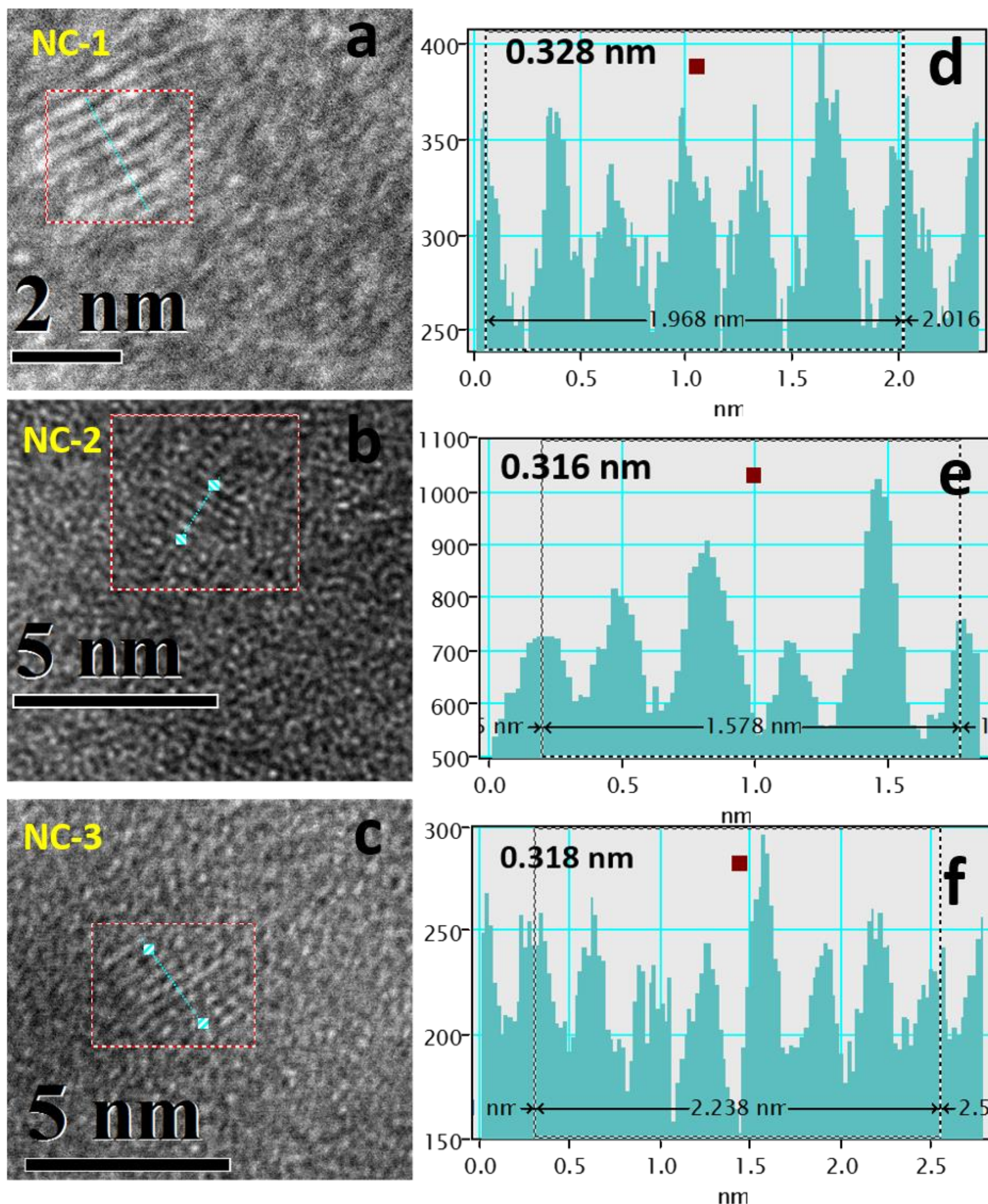

Figure S1: *High resolution transmission electron micrographs of samples exhibiting 1.4 nm mean diameter Si-Sn NCs and their corresponding lattice fringes profile.*

Figure S2 reports line profile analysis of HR-TEM images of three NCs related to samples that exhibited NCs with 1.7 nm mean diameter. The line profile analysis has produced an average lattice spacing of 0.193 nm (220), 0.319 nm (111) and 0.197 nm (220) for NC-1, NC-2 and NC-3 respectively.

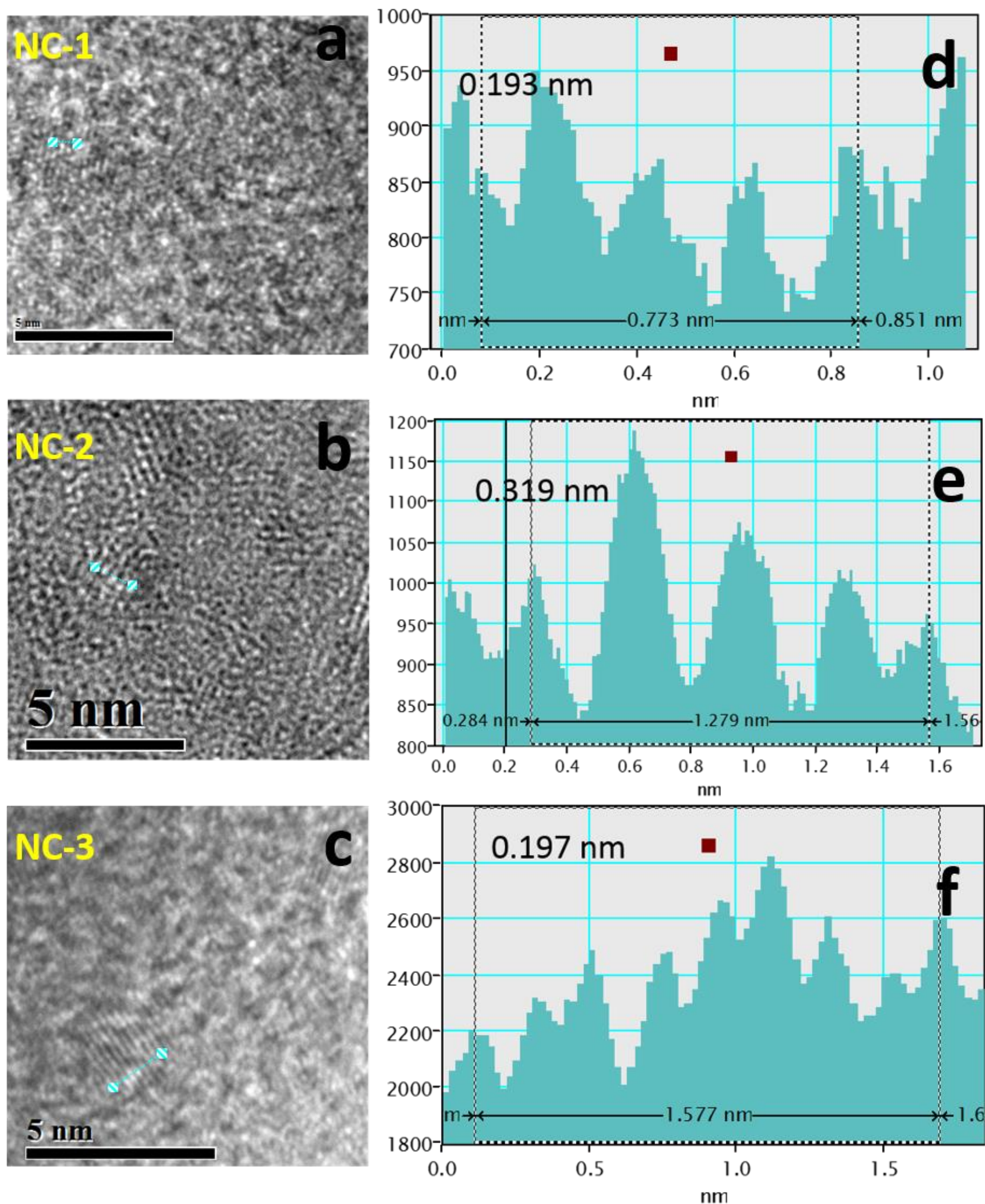

Figure S2: *High resolution transmission electron micrographs of 1.71 nm Si-Sn NCs and their corresponding lattice fringes profile.*

Figure S3 reports line profile analysis of HR-TEM images of three NCs corresponding to samples with NCs with mean diameter of 2.2 nm. The line profile analysis suggests an average lattice spacing of 0.198 nm (220), 0.194 nm (220) and 0.193 nm (220) for NC-1, NC-2 and NC-3 respectively.

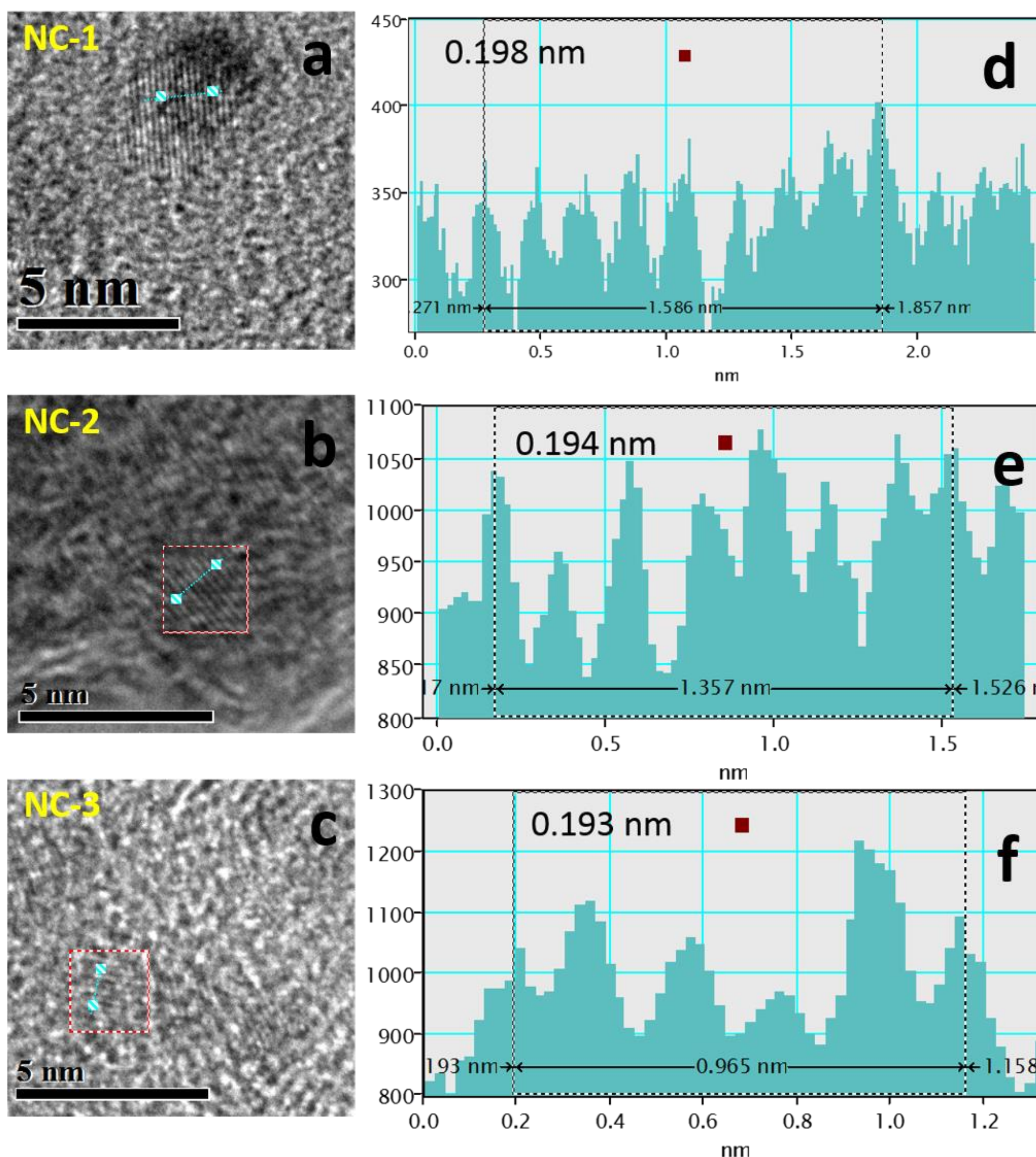

Figure S3: *High resolution transmission electron micrographs of 2.23 nm Si-Sn NCs and their corresponding lattice fringes profile.*

The results of figure S1-S3 are summarized in table S1, which shows values for the lattice spacing in the range 0.316-0.333 nm for the (111) plane and in the range 0.193-0.204 nm for the (220) plane. The values are all larger than the standard bulk Si lattice spacing values, i.e. 0.313 nm for (111) and 0.192 nm for (220), and also larger than the smallest elemental Si NCs (1.5 nm) that we simulated, which is expected to have the largest expansion of the lattice spacing and resulted with a value of 0.315 nm for the (111) plane. Theoretical calculations also show a trend in larger lattice spacing values for the cluster-doped NCs, corroborating with the experimental results of table S1.

Table S1: *Lattice spacing and lattice constant of Si-Sn NCs.*

1.4 nm mean diameter Si-Sn nanocrystals			
	(*hkl*)	**Average lattice spacing, d_{hkl} (nm)**	**Lattice parameter, *a* (nm)**
NC-1	(111)	0.328	0.568
NC-2	(111)	0.316	0.546
NC-3	(111)	0.318	0.551
1.7 nm mean diameter Si-Sn nanocrystals			
	(*hkl*)	**Average lattice spacing, d_{hkl} (nm)**	**Lattice parameter, *a*, (nm)**
NC-1	(220)	0.193	0.546
NC-2	(111)	0.319	0.553
NC-3	(220)	0.197	0.557
2.2 nm mean diameter Si-Sn nanocrystals			
	(*hkl*)	**Average lattice spacing, d_{hkl} (nm)**	**Lattice parameter, *a* (nm)**
NC-1	(220)	0.198	0.560
NC-2	(220)	0.194	0.549
NC-3	(220)	0.193	0.546

The average lattice spacing (d_{hkl}) measured from each NC is reported in the table S1. The lattice parameter for each NCs have been determined by using the relation,

$$a_{SiSn} = d_{hkl}\sqrt{h^2 + k^2 + l^2} \qquad \textit{Equation S1}$$

where d_{hkl} is the lattice spacing, a_{SiSn} is the lattice parameter and h, k, l are the lattice planes.

SI-B. Oxidation behaviour of Si-Sn NCs

Understanding oxidation of NCs, particularly Si and Si-based NCs, is of great importance for their successful integration and enhanced performance in applications. Oxidation of Si NCs is very common and it is therefore important to understand the role of different environments affecting the oxidation behaviour of Si-Sn NCs. In this work, the oxidation behaviour of Si-Sn NCs was studied in air, toluene and water. The oxidation of Si-Sn NCs was studied by monitoring the changes in the FTIR and XPS spectra over a number of days.

Figure S4a-i show FTIR spectra for the Si-Sn NCs of different mean diameter exposed to air, water or toluene up to 168 h. The intensity of Si-H_2 (~850 cm^{-1}) is higher than Si-O-Si (~1050 cm^{-1}) peak in freshly prepared samples for all sizes. With time, the Si- H_2 bond is replaced by Si-O-Si. In order to assess the time evolution of the oxidation process, the ratio between the Si-O-Si peak and the Si-H_2 has been monitored, which provides a trend of the loss of surface hydrogen bonds in favour of oxygen-based bonds. For 1.4 nm diameter Si-Sn NCs the ratio is initially 0.73 and increases with time to 0.91, 1.46 and 0.98 in air, water and toluene, respectively (Figure S4a-c). For 1.7 nm Si-Sn NCs the ratio increases from 0.5 to 0.91, 0.95 and 0.92 in air, water and toluene respectively (Figure S4d-f). In the case of 2.2 nm, the ratio increases from 0.54 to 0.95, 1.05 and 1.04 in air, water and toluene respectively as shown in Figure S4g-i. It is clear now that the oxidation peak intensity increases with time due to exposure to air, water and toluene for all samples. The oxidation rate is much faster in water environment as compared to air and toluene environment in all samples. Further, smaller NCs showed a higher degree of oxidation immediately after synthesis (see 0.73 ratio at the start). This could be due to higher surface energy due to the NC curvature and easier back-bond oxidation. However, the smaller NCs may offer some geometrical constraints which then slow down and limit the oxidation.[1] Interestingly, the oxidation rate in ambient environment is slightly lower than that in toluene environment. The justification for this lies in the changes happening in the hydrophobic characteristic of Si-Sn NCs.

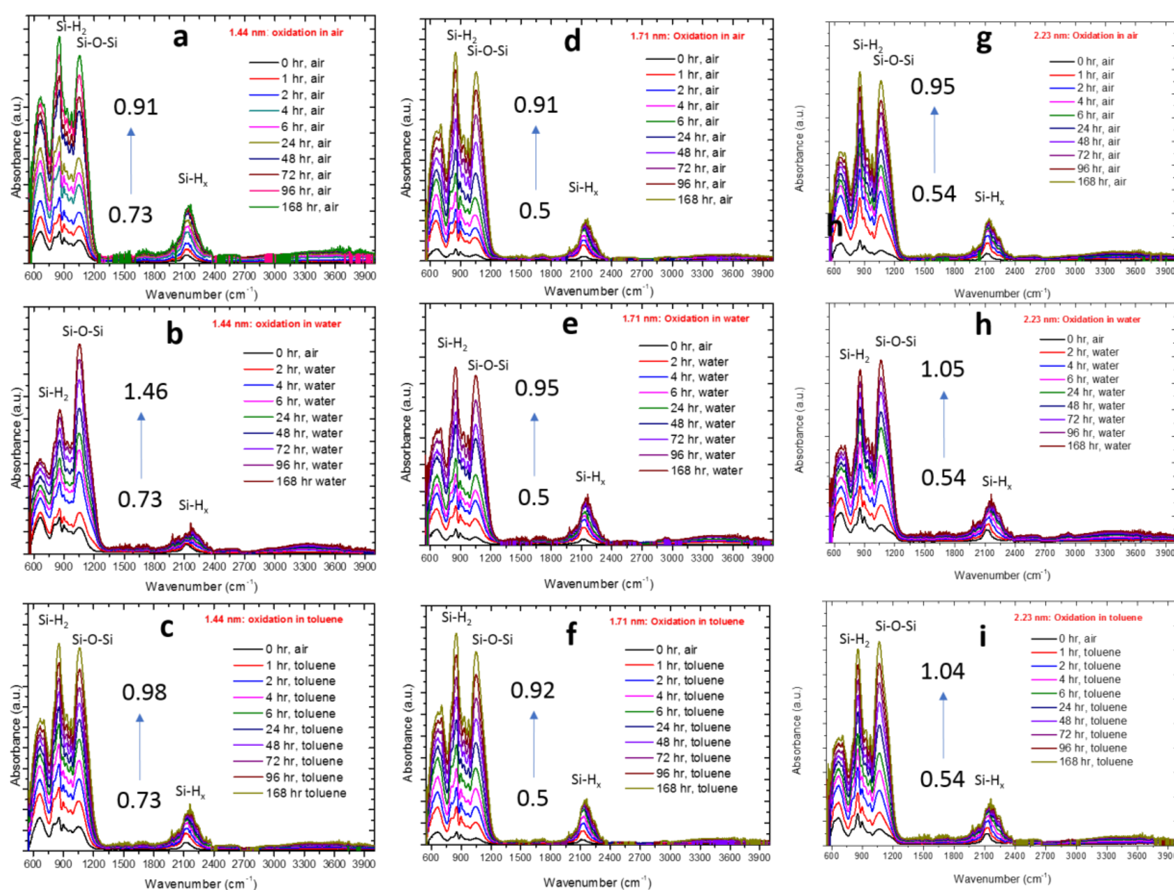

Figure S4: *(a-c) Time-dependent oxidation behaviour of hydrogen-passivated 1.4 nm silicon-tin (Si-Sn) nanocrystals (NCs) in air, water and toluene environmental conditions; (d-f) Time-dependent oxidation behaviour of hydrogen-passivated 1.7 nm silicon-tin (Si-Sn) nanocrystals (NCs) in air, water and toluene environmental conditions; (g-i) Time-dependent oxidation behaviour of hydrogen-passivated 2.2 nm silicon-tin (Si-Sn) nanocrystals (NCs) in air, water and toluene environmental conditions. The increase in ratios between Si-O-Si and SiH_2 from 0 hr to 168 hr is also indicated in (a-i). All the FTIR spectra are stacked with Y-offset (cumulative) in OriginPro for the purpose of enhance readability.*

Figure S5a-c summarizes the trends in the oxidation characteristics of Si-Sn NCs through the intensity ratios between Si-O-Si (~1050 cm^{-1}) and SiH_2 (~850 cm^{-1}) peak from the FTIR spectra. There is a sharp rise in the ratio for the smallest NCs (1.4 nm) at the very initial moments after synthesis, compared to the larger NCs (1.7 nm and 2.2 nm), which appear to have a more constant oxidation rate. The oxidation rate for the smallest NCs then slows down and after 168 h in air and toluene, all NCs of the different sizes appear to have a similar degree of oxidation. However, in water, the larger NCs present a similar trend in the ratio values while the smallest NCs appear to be particularly prone to oxidation with the highest values for the Si-O-Si and SiH_2 ratios.

Monitoring the oxygen back-bond (O-SiH) provides further clues to the oxidation behaviour and Figure S5d-f reports on the normalized intensity of the corresponding peak. The maximum of back-bond oxidation for the 1.4 nm Si-Sn NCs is reached after a longer time compared to the larger NCs and with the largest NCs (2.2 nm) reaching its maximum within the first few hours of exposure to air, toluene and water. This suggest that while the oxidation of the larger NCs (1.7 nm and 2.2 nm) may progress as expected through back-bond cleavage and oxidation, the smallest NCs are quickly oxidized at the surface by H-bonds replacement and back-bond oxidation taking place at a slower pace.

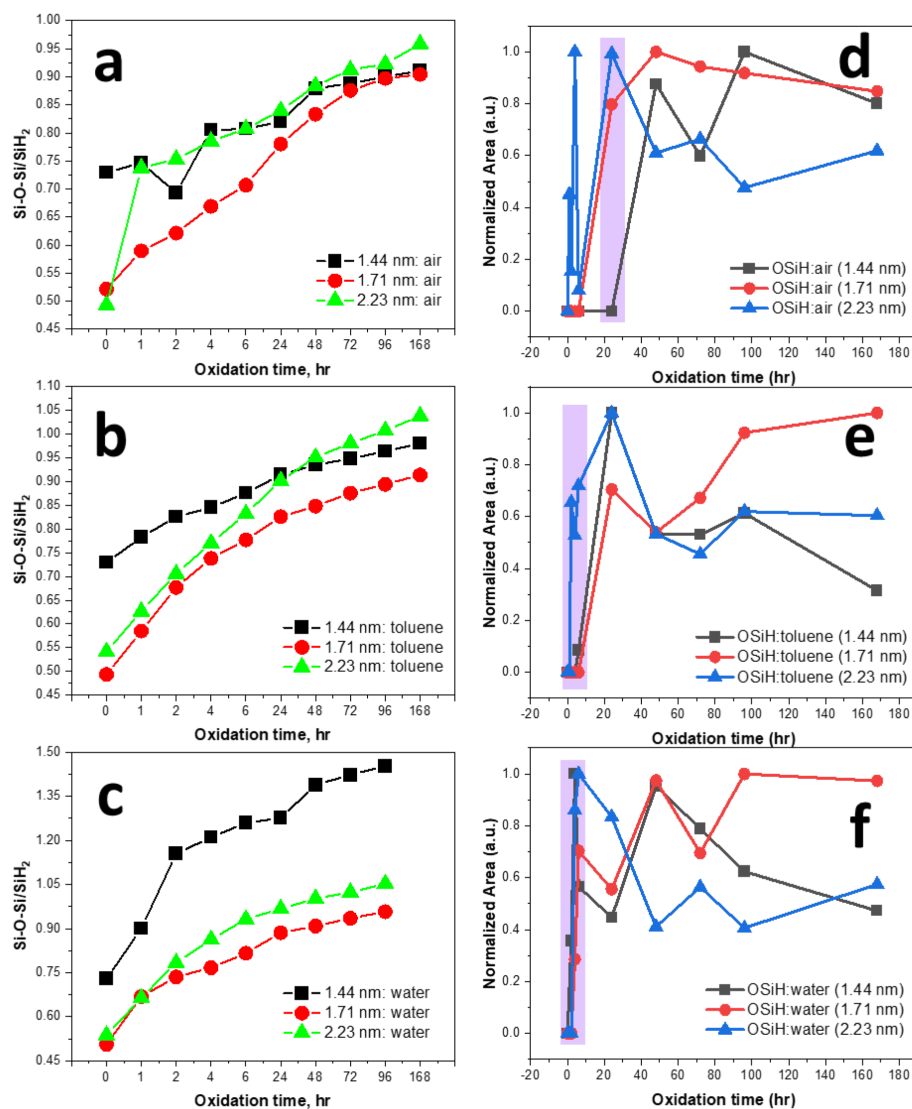

Figure S5: *(a-c) The changes in the Si-O-Si/SiH2 ratios, deduced from FTIR signal, over oxidation time in air, toluene and water respectively; (d-f) The behaviour of OSiH back-bond oxidation upon increasing the oxidation time in oxidizing media such as air, toluene and water respectively.*

To further confirm these findings, we also deconvoluted the SiH_x peak around 2100 cm^{-1} into Si-H, Si-H_2, Si-H_3 and O-SiH using Gaussian peak fitting in Fityk 0.9.8. The normalized area of these peaks to the total area is then plotted versus time in the form of a bar chart diagrams as shown in figures S6-S8.

The peak area of both the Si-H_2, Si-H_3 peak decreases over time for all samples in all the environmental conditions. However, the reduction is much faster in toluene and water environment which is due to the changes in the hydrophobic nature of the surface and most importantly the formation of O-SiH_x much earlier. The absence of O-SiH (2226 cm^{-1}) bond in 1.4 nm Si-Sn NCs before 48 h compared to 1.7 nm and 2.2 nm Si-Sn NCs indicates the superior stability against back-bond oxidation in smaller Si-Sn NCs as shown in Figure S6a-c.

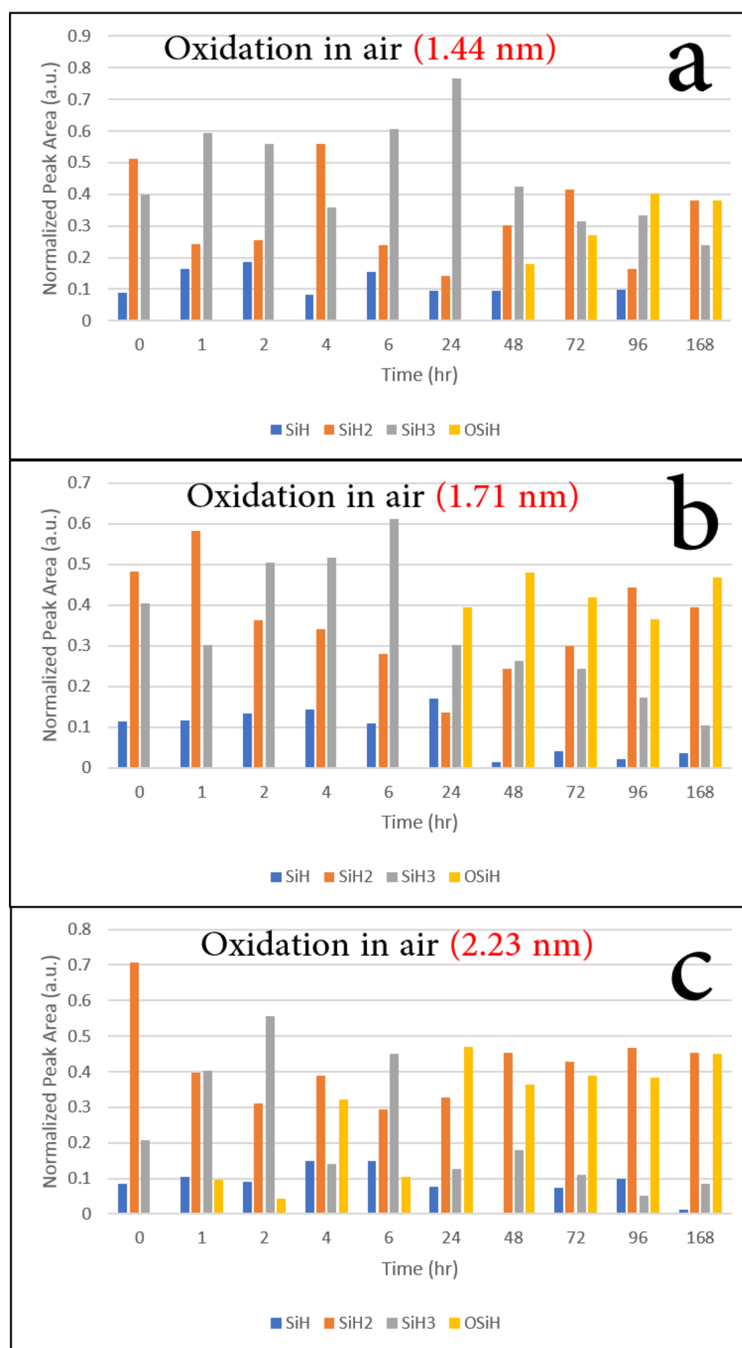

Figure S6: *(a-c) The Bar chart diagrams showing the time-dependent changes in the deconvoluted peak areas of SiH (1987 cm^{-1}), SiH_2 (2121 cm^{-1}), SiH_3 (2165 cm^{-1}) and OSiH (>2226 cm^{-1}) of 1.4 nm, 1.7 nm and 2.2 nm alloyed silicon-tin (Si-Sn) nanocrystals (NCs) extracted from their corresponding Fourier Transform Infrared (FTIR) spectra taken after exposing Si-Sn NCs in air environment respectively.*

Figure S7 shows the oxidation behaviour of Si-Sn NCs after exposing them to the toluene environment. The Si-H remains constant for all samples in toluene environment. While the SiH_2 and SiH_3 peak area decreases with time. The O-SiH back-bond formation starts after 6 h for 1.44 nm and after 24 h for 1.71 nm whereas it appears within 2 h of exposure to toluene environment for the case of 2.23 nm Si-Sn NCs as shown in Figure S7a-c. These findings suggest that the back-bond oxidation attacks the Si-Si bonds which is then replaced with O-Si. The oxidation resistance of larger Si-Sn NCs is poor in this environment compared to smaller Si-Sn NCs. Hence, the surface of smaller Si-Sn NCs has not completely been replaced by oxygen even after seven days.

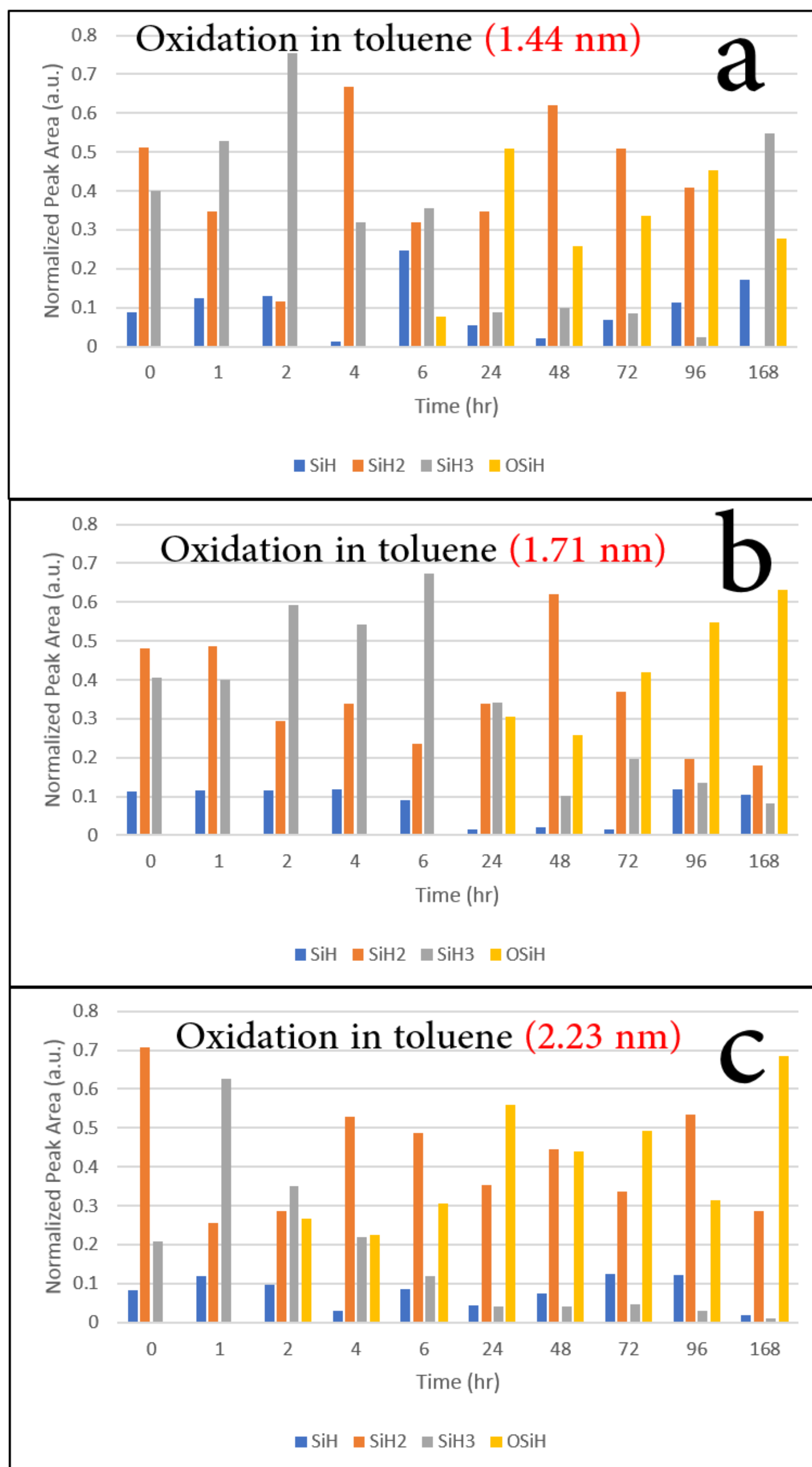

Figure S7: *(a-c) The Bar chart diagrams showing the time-dependent changes in the deconvoluted peak areas of SiH (1987 cm-1), SiH2 (2121 cm-1), SiH3 (2165 cm-1) and OSiH (>2226 cm-1) of 1.44 nm, 1.71 nm and 2.23 nm alloyed silicon-tin (Si-Sn) nanocrystals (NCs) extracted from their corresponding Fourier Transform Infrared (FTIR) spectra taken after exposing Si-Sn NCs in toluene environment respectively.*

Figure S8a-c shows the oxidation behaviour of Si-Sn NCs exposed to water environment. The Si-H remains constant for all samples in water environment. While the SiH_2 and SiH_3 peak area decreases

with time. The O-SiH back-bond formation starts just after 2 h of exposure in 1.4 nm Si-Sn NCs to water environment. Whereas it appears after 4 h in both 1.7 nm and 2.2 nm Si-Sn NCs. This concludes that smaller Si-Sn NCs are not stable in water environment compared to larger NCs. However, the stability of these NCs is poor in water environment due to the breakage of Si-H bonds in a much faster rate compared to toluene and air environment.

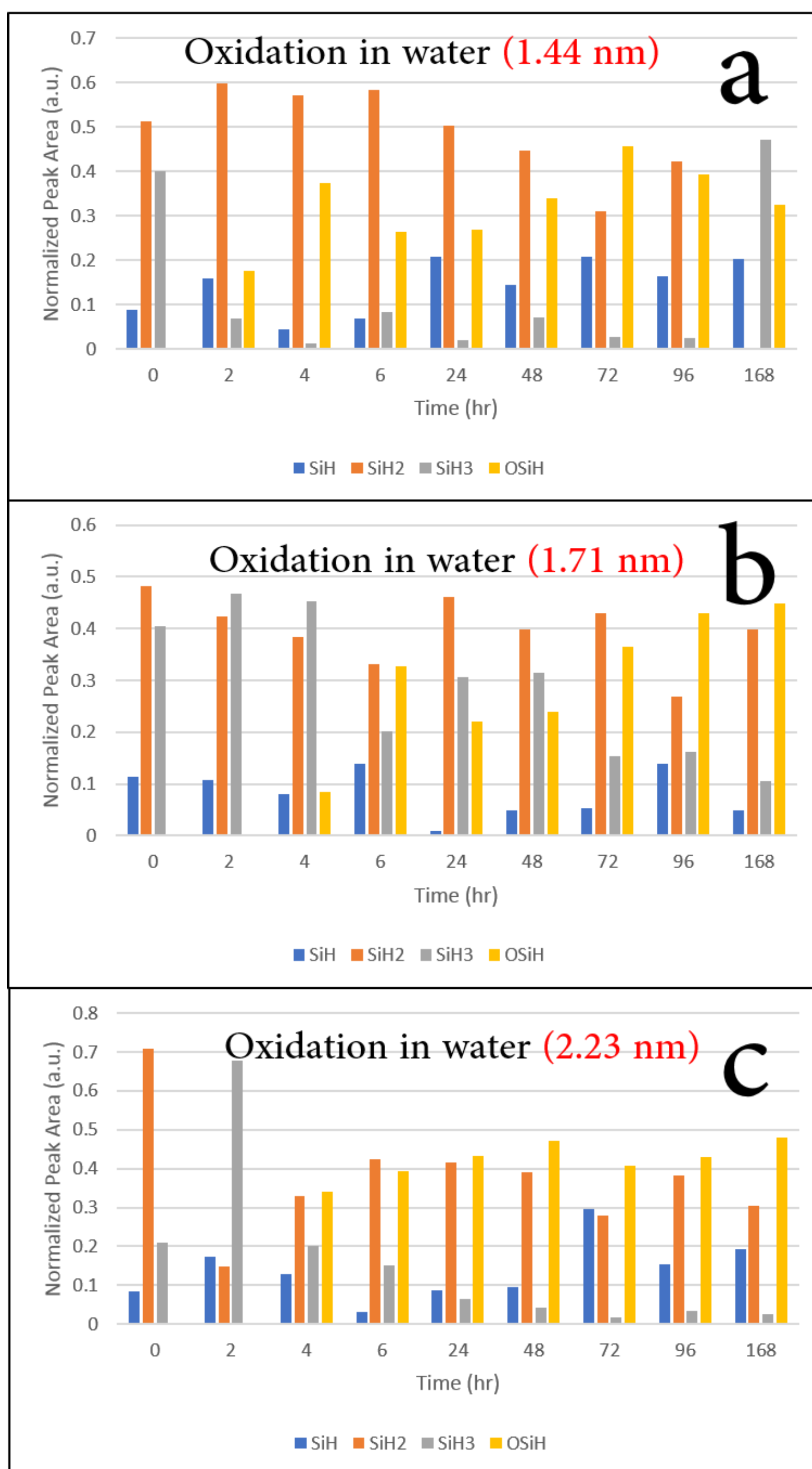

Figure S8: *(a-c) The Bar chart diagrams showing the time-dependent changes in the deconvoluted peak areas of SiH (1987 cm-1), SiH2 (2121 cm-1), SiH3 (2165 cm-1) and OSiH (>2226 cm-1) of 1.44 nm, 1.71 nm and 2.23 nm alloyed silicon-tin (Si-Sn) nanocrystals (NCs) extracted from their*

corresponding Fourier Transform Infrared (FTIR) spectra taken after exposing Si-Sn NCs in water environment respectively.

The FTIR analysis has shown that exposure to air contribute to the slowest oxidation for all Si-Sn NCs. In order to gain further guidance on the state of oxidation of the Si-Sn NCs during other measurements (e.g. to determine band energy levels), XPS analysis was also carried out on the Si-Sn NCs exposed to air up to 7 days. The oxidation of Si-Sn NCs in ambient air were studied by monitoring the changes in the Si 2p and Sn 4d high resolution spectra over time as shown in Figure S9-11. The oxidation in Si-Sn NCs is found to be mainly due to the oxidation of Si because the Si 2p peaks shifts to higher binding energy over time, while the Sn 4d peak is fairly constant.

Figure S9 shows the Si 2p and Sn 4d spectra of 1.4 nm Si-Sn NCs taken just after sample preparation (fresh), after 1-day and after 7-days. The Si-Si and Si-H/Si-Sn and Si^{2+} peaks can be seen in fresh samples which oxidises further to incorporate the Si^{+1} component and replacing some of the Si-H/Si-Si bonds as can be seen in the spectra taken after 1-day (Figure S9b). The Si-Si and Si-H/Si-Sn peak is greatly reduced in 7-days due to increase in the oxidation. The higher oxidation states of Si (i.e. Si^{2+} and Si^{3+}) become stronger as can be seen in Figure S9c. No major changes are observed for Sn^0 and Sn^{2+} in Sn 4d spectra after 1-day and after 7-days (Figure S9d-f).

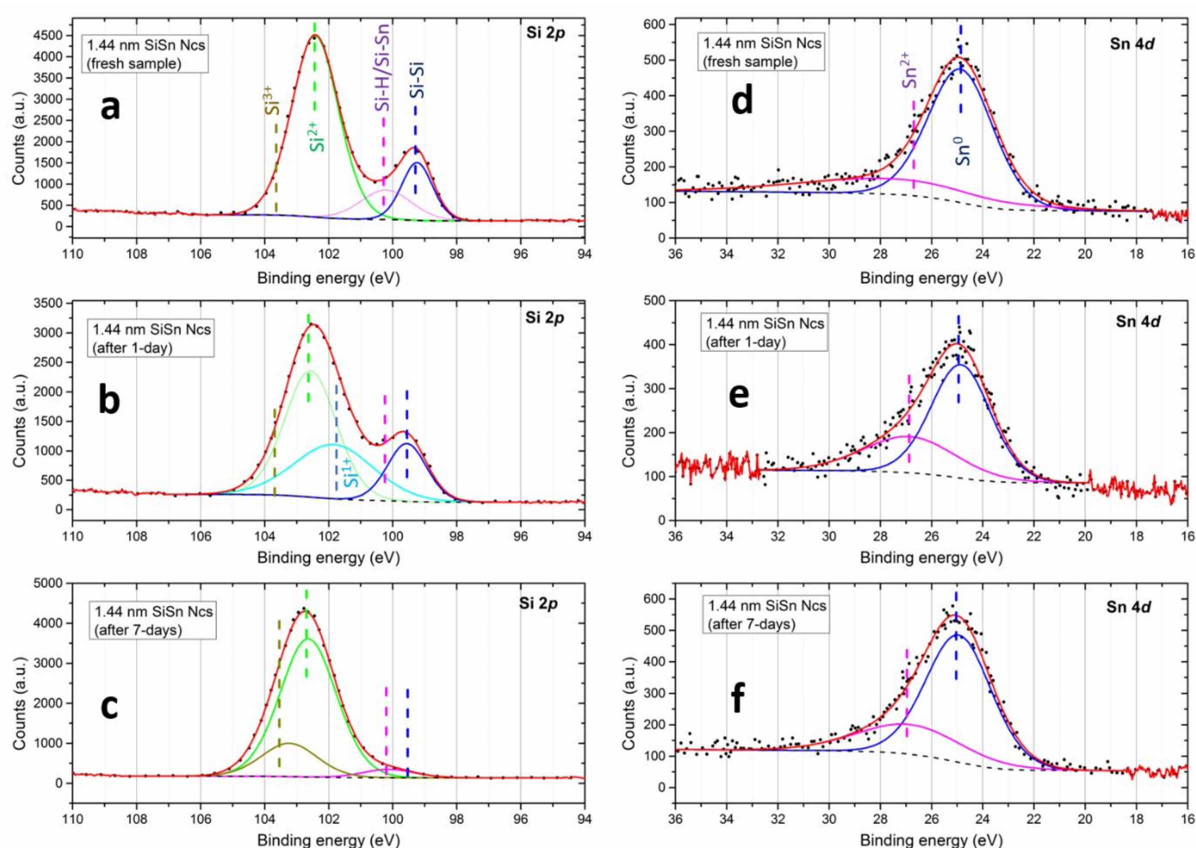

Figure S9: *(a-f) The time dependent evolution of Si 2p and Sn 4d X-ray photoelectron spectroscopy (XPS) spectra of 1.44 nm alloyed silicon-tin nanocrystals.*

Figure S10 shows the Si 2p and Sn 4d spectra of 1.7 nm Si-Sn NCs. The Si-Si and Si-H/Si-Sn and Si^{2+} peaks become all weaker after 1-day and after 7-days due to the appearance of a stronger Si^{3+} peak at around 103 eV. This suggests a rapid oxidation rate in 1.71 nm Si-Sn NCs compared to 1.44 nm Si-Sn NCs. Similarly to the smaller NCs, no significant changes are found in Sn^0 and Sn^{2+} in Sn 4d spectra.

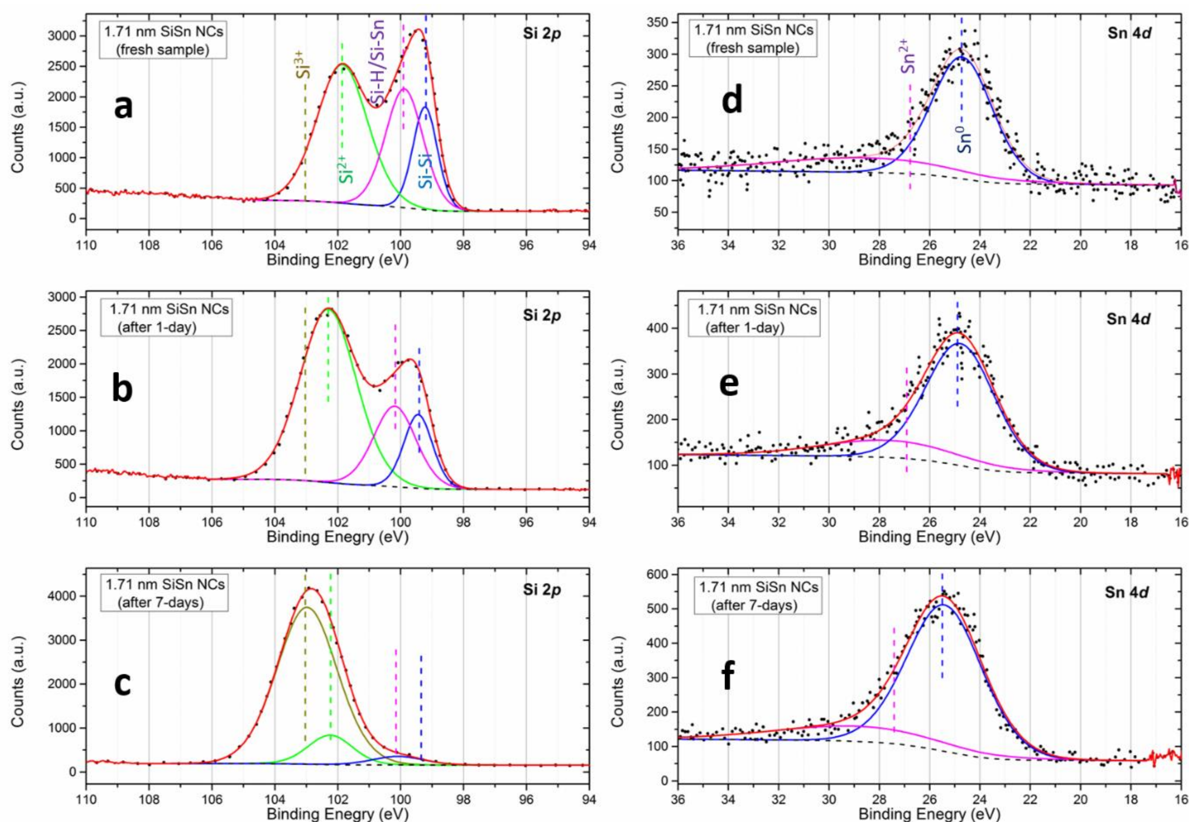

Figure S10: *(a-f) The time dependent evolution of Si 2p and Sn 4d X-ray photoelectron spectroscopy (XPS) spectra of 1.71 nm alloyed silicon-tin nanocrystals.*

Figure S11 shows the Si 2p and Sn 4d spectra of 2.2 nm Si-Sn NCs. The Si-Si/ Si-H/Si-Sn peak are weakened over time (from 1-day to 7-days) due to appearance of suboxides peaks of Si. For instance, the Si^{2+} peak appears after 1-day which is then weakened by the appearance of Si^{3+} peak at 103.36 eV suggesting that the oxidation is quicker in 2.2 nm Si-Sn NCs compared to 1.4 nm Si-Sn NCs. Further, the Sn^{0} and Sn^{2+} observe no changes over time suggesting that the oxidation in Si-Sn NCs is not due to the oxidation of Sn.

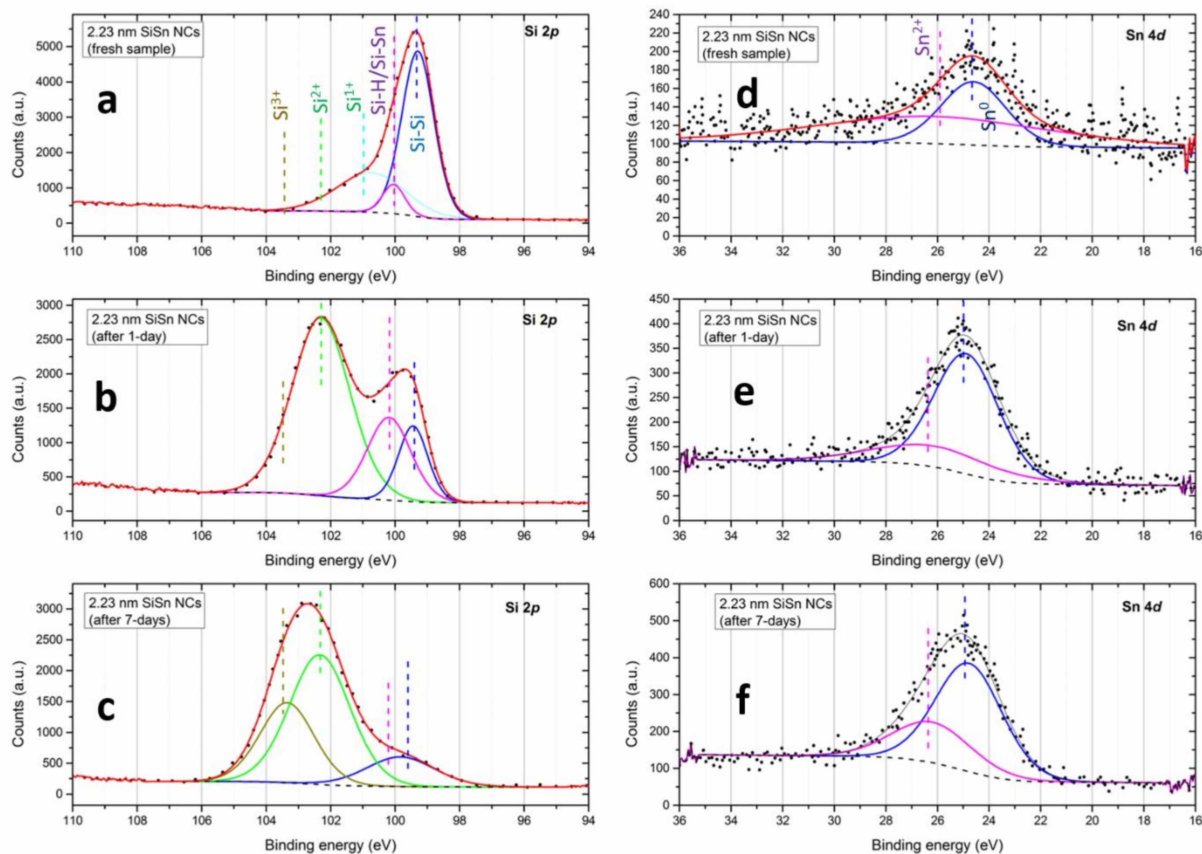

Figure S11: *(a-f) The time dependent evolution of Si 2p and Sn 4d X-ray photoelectron spectroscopy (XPS) spectra of 2.23 nm alloyed silicon-tin nanocrystals.*

A summary of the oxidation trend is reported in Figure S12 where the area ratio of the deconvoluted peaks in Si 2p representing unoxidized Si (Si-Si, Si-H/SiSn) and oxidized Si (Si^{+1}, Si^{+2} and Si^{+3}) are plotted in the form of bar chart diagram. It can be seen that smaller NCs are prone to surface oxidation more than the larger NCs.

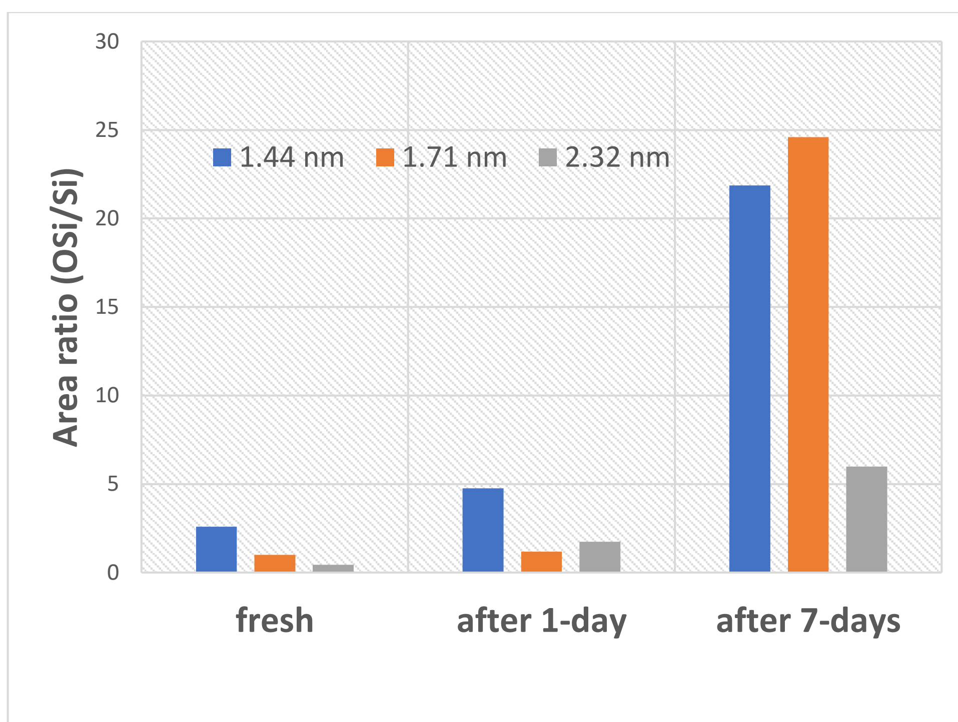

Figure S12: *The bar chart diagram showing the time-dependent changes in the peak areas of the deconvoluted Si 2p peak in high resolution XPS for 1.44 nm, 1.71 nm and 2.32 nm respectively.*

Si-Sn NCs synthesized through atmospheric pressure plasma are found to be highly hydrophobic as shown in Figure S13. The hydrophobicity is due to the H-terminations on the surface of Si-Sn NCs. Both the FTIR and XPS confirms the presence of H-terminations on the surface of Si-Sn NCs. Freshly prepared samples of Si-Sn NCs are partially oxidized due to exposure to ambient environment. The oxidation behaviour of Si-Sn NCs is very much dependent on the moisture present in the air which helps in breaking the Si-Si/Si-H bonds to initiate the oxidation process. The oxidation rate, in air, in smaller Si-Sn NCs (1.44 nm), is very slow compared to the larger Si-Sn NCs (1.71 nm and 2.23 nm) as confirmed by both FTIR and XPS. Furthermore, it is clear now from both the time resolved FTIR and XPS spectra, that the oxidation of Si-Sn NCs is partial and proceeds due to the attack of oxygen atoms preferentially on the Si-Si back-bonds with major contribution from the moisture present in the air. Sn has shown no significant role in the oxidation behaviour of the Si-Sn NCs as confirmed by both the FTIR and XPS.

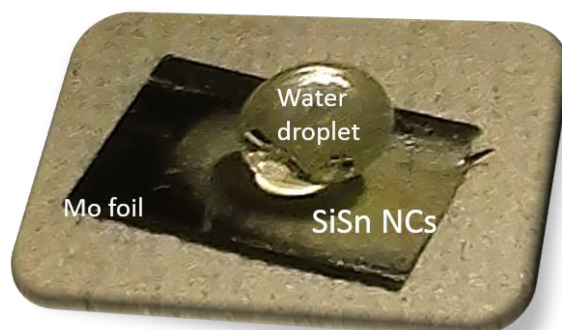

Figure S13: *A digital photograph of a water droplet staying on the surface of Si-Sn NCs revealing the hydrophobic nature of Si-Sn NCs. The Si-Sn NCs were deposited on molybdenum foil directly from the atmospheric pressure plasma.*

Overall FTIR and XPS analysis has portrayed a consistent picture of the Si-Sn NCs, confirming the presence of Sn throughout the samples and clear but consistent differences among samples that exhibited different mean diameters.

All samples shortly after synthesis (e.g. < 1 day) did present a degree of oxidation however this was limited and where much of the NC surface still presented H-terminations (Figure S5a, S6a, S7a and S8a) with no back-bond oxidation present (Figure S6). The smaller NCs (1.4 nm) presented a fast surface-restricted oxidation, possibly through direct replacement of surface H-bonds with oxygen-based bonds (e.g. Figure S12). Back-bond oxidation is slower in smaller NCs but more predominant in larger NCs. Oxidation takes place exclusively at the Si-sites indicating that Sn atoms are not at the surface. We can conclude that sample handling in air minimizes oxidation compared to storage in water or toluene. Handling and measurements carried out within 1 day from synthesis can be considered mainly H-terminated with a low degree of oxidation.

SI-C. Evaluation of band energy levels

Figure S14a shows the photoemission versus energy graph. A clear threshold of photoemission can be seen in our samples. Based on Fowler theory,[2] the cube-root photo-response plots are reported in Figure S14b. From the linear extrapolation method, the valence band maximum values obtained for 1.4 nm, 1.7 nm and 2.2 nm are -5.84 eV, -5.89 eV and -5.94 eV respectively.

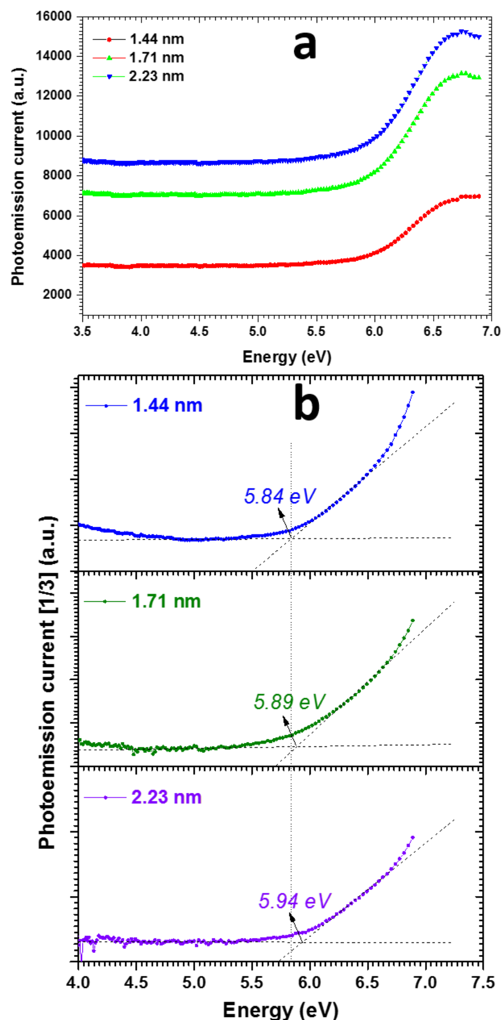

Figure S14: *(a) Air-photoemission spectra of Si-Sn NCs showing the photoemission threshold edge; (b) the cube root photoemission spectra with fit lines revealing the valence band maximum of the Si-Sn NCs.*

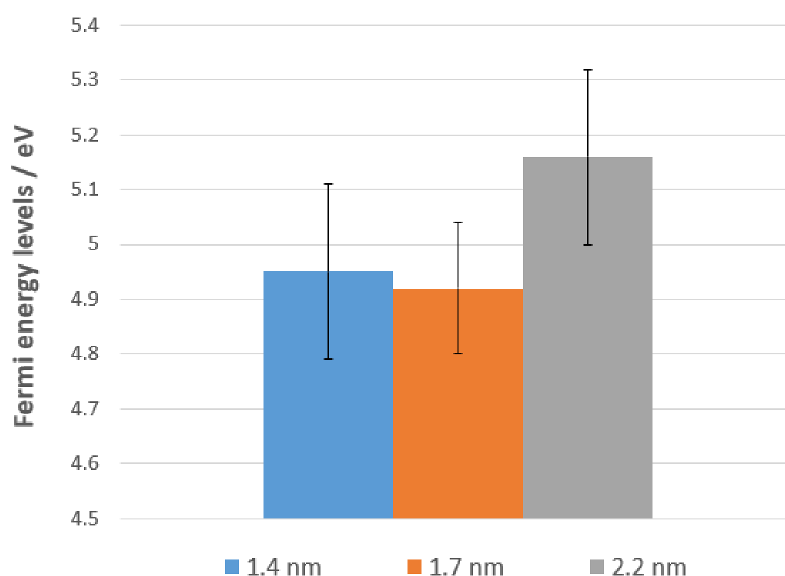

Figure S15: *Fermi energy levels of Si-Sn NCs obtained by Kelvin Probe.*

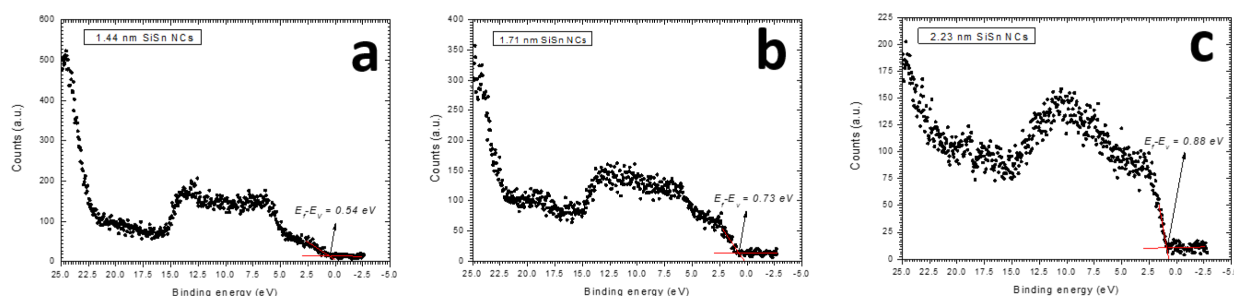

Figure S16: *(a-c) Valence band spectra from x-ray photoelectron spectroscopy showing the onset of the signal in 1.4 nm, 1.7 nm and 2.2 nm Si-Sn nanocrystals. The difference between the valence band maximum (E_V) and the Fermi level (E_F) is obtained.*

Figure S17a shows the surface photovoltage spectroscopy (SPS) measurements for 1.4 nm, 1.7 nm and 2.2 nm NCs. The SPS spectra show very broad SPS region for all samples. Also, the signal for 1.7 nm and 2.2 nm are weaker than 1.4 nm Si-Sn NCs. The SPS spectra bends downwards in both case and hence indicates p-type behaviour in Si-Sn NCs. Figure S17b-d shows the derivative of the corresponding SPS spectra showing peak maxima at 1.65 eV, 1.82 eV and 1.93 eV for 1.4 nm, 1.7 nm and 2.2 nm Si-Sn NCs.

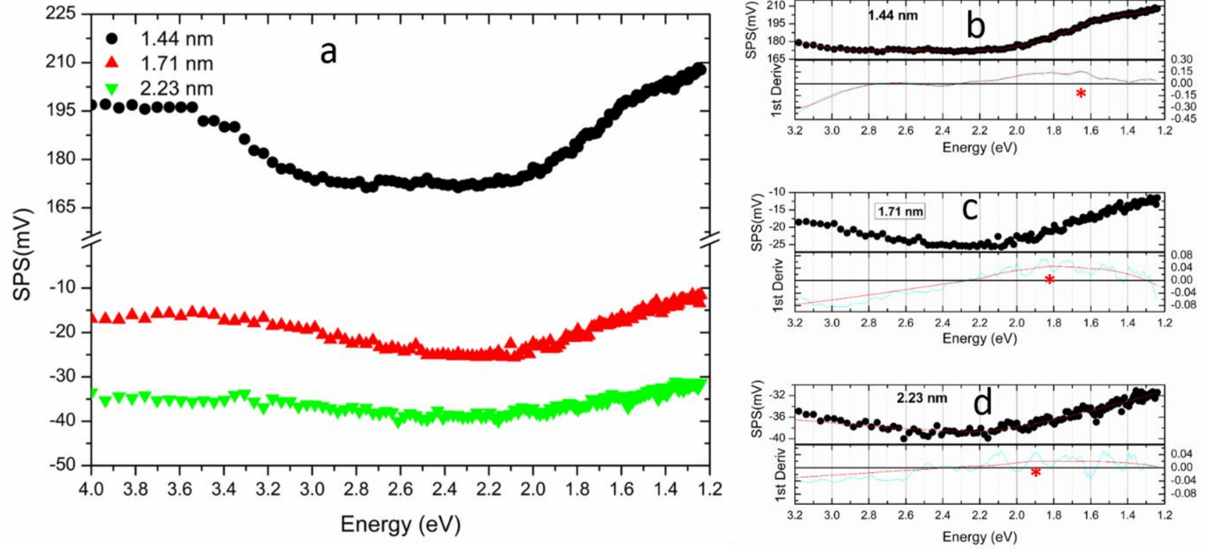

Figure S17: *(a) Surface Photovoltage Spectra (SPS) measured in an air photoemission Kelvin Probe system for 1.4 nm, 1.7 nm and 2.2 nm silicon-tin (Si-Sn) nanocrystals (NCs) showing p-type behaviour; (b-d) SPS spectra and their first derivatives resulting in an approximated bandgap of 1.65 eV, 1.82 eV and 1.93 eV for 1.4 nm, 1.7 nm and 2.2 nm Si-Sn NCs respectively. The smoothing of the spectra in (b-d) is done in OriginPro 9 by using Savitzky-Golay (S-G) filtering method.*

The bandgap was also estimated with Tauc plots from ultraviolet-visible spectroscopy (UV-Vis) measurements using a PerkinElmer spectrometer equipped with a 150 mm integrating sphere, which allowed the measurements of both transmittance (T) and transmittance and any light scattered in different directions from the nanocrystals ($T+S$). Because of the small thickness of the sample and the rough surface morphology we are unable to separate surface phenomena such as pure reflection from other types of light interactions and therefore we considered any light that is not transmitted and not absorbed as scattering (S) distributed through the sample. Samples for UV-Vis measurements were deposited directly from plasma onto quartz substrates.

The transmittance T is written as

$$\boldsymbol{T = \left(\frac{I(L)}{I_0}\right) = e^{-\mu L}} \qquad \text{(Equation S2)}$$

Where I_0 is the intensity of the incident light beam, $I(L)$ is the light intensity transmitted through the sample, μ is the extinction coefficient and L stands for the optical path length or thickness of the sample.

The light absorbed $I_a(L)$ by the sample can be written as

$$\boldsymbol{I_a(L) = \int_0^L I(x)\mu_a dx} \qquad \text{(Equation S3)}$$

and using equation S3 we can write

$$\boldsymbol{I_a(L) = \int_0^L I_0 e^{-\mu x}\mu_a dx}. \qquad \text{(Equation S4)}$$

Solving equation S4 we get

$$\boldsymbol{I_a(L) = I_0\frac{\mu_a}{\mu}\left(1 - e^{-\mu L}\right)}. \qquad \text{(Equation S5)}$$

The absorptance of a sample (Abs) can be written as

$$\boldsymbol{\frac{I_a(L)}{I_0} = Abs = 1 - (T + S)} \qquad \text{(Equation S6)}$$

Therefore, equation S6 can be re-written as

$$\mathbf{1} - (\boldsymbol{T} + \boldsymbol{S}) = \frac{\boldsymbol{\mu_a}}{\boldsymbol{\mu}}\left(\mathbf{1} - \boldsymbol{e}^{-\boldsymbol{\mu L}}\right) \qquad (\textit{Equation S7})$$

and using equation S2

$$\boldsymbol{\mu_a} = \boldsymbol{\mu}\frac{\mathbf{1}-(\boldsymbol{T}+\boldsymbol{S})}{(\mathbf{1}-\boldsymbol{e}^{-\boldsymbol{\mu L}})} = \frac{-\ln \boldsymbol{T}}{\boldsymbol{L}}\frac{\mathbf{1}-(\boldsymbol{T}+\boldsymbol{S})}{(\mathbf{1}-T)} \qquad (\textit{Equation S8})$$

Equation S8 provides a way to calculate the absorption coefficient on the basis of the measurements T and $T+S$. We should note that while we do not have a value for L, this is not required to determine the bandgap from Tauc plots (Figure S18). The linear fitting was performed in OriginPro 9 by selecting solely the linear portion in each spectrum. The Tauc plots then resulted in the bandgaps of 1.6 eV, 1.8 eV and 2.4 eV for 1.4 nm, 1.7 nm and 2.2 nm respectively.

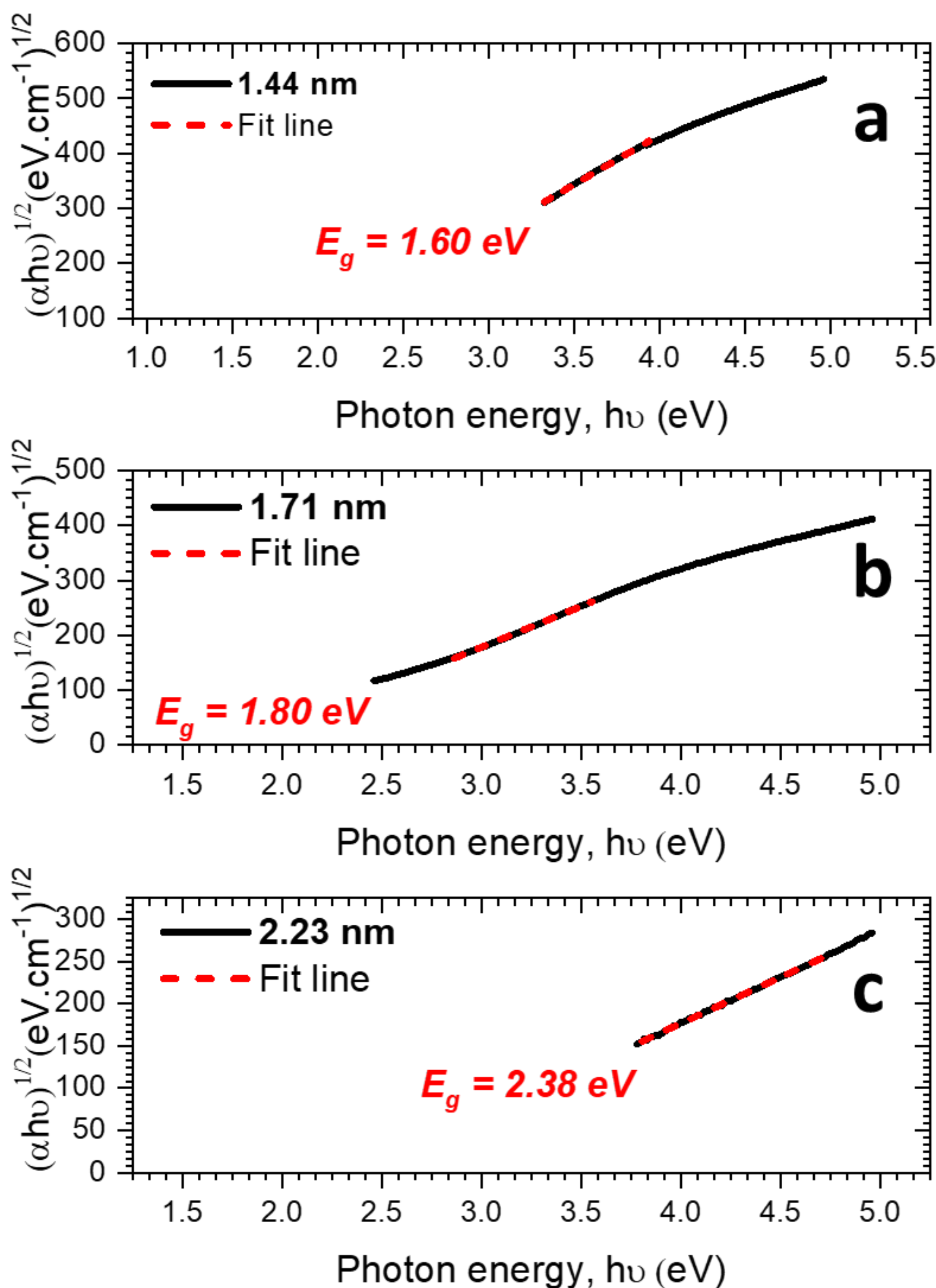

Figure S18: *(a-c) Tauc plots of the transmittance spectra of silicon-tin (Si-Sn) nanocrystals (NCs) with mean diameters of around 1.4 nm, 1.7 nm and 2.2 nm along with the linear extrapolation that resulted in bandgaps of 1.60 eV, 1.80 eV and 2.38 eV respectively.*

The values from SPS and UV-Vis follow the same trend and are also very close to each other for NCs with diameter of 1.4 nm and 1.7 nm. The larger NCs (2.2 nm diameter) show different values for the bandgap depending on the measurement, however this is probably a consequence of the noisy signals.

The Si-Sn NCs bandgap is also compared with the bandgap values reported in the literature which is shown in Figure 19. The Si-Sn nanoparticles (3 nm) reported in the literature resulted in an optical bandgap of around 0.81 eV with 12% Sn.[3] The concentration of Sn reported for the bandgap reduction or direct to indirect transition in Si-Sn is still debated in the literature.[4–7] It is to be noted

here, that the change in the bandgap in Si-Sn is significant at higher Sn concentrations in our theoretical calculations while such bandgap change becomes significant in much lower concentrations of Sn in our experimental results. This could be due to the interplay between quantum confinement and compositional/straining effects influencing the mismatch between our theoretical predictions and experimental results.

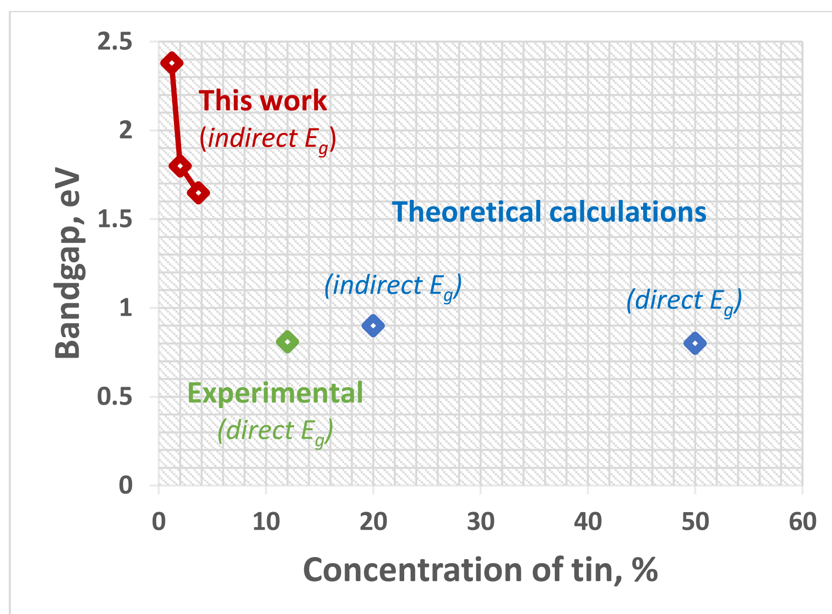

Figure S19: *a comparison of the bandgap of our Si-Sn NCs with the reported bandgap values in the literature* [3,8]*. We should note that other NCs in the literature were reported as alloys of Si and Sn and not through cluster doping.*

All these measurements provide details of the energy band levels, which are summarized in table S2. The bandgap values have been produced by SPS and Tauc plots. The Fermi level was measured by Kelvin probe measurements. The XPS valence band spectra produced the difference between valence band maximum (VBM) and the Fermi level and combining these with the Kelvin probe measurements, the VBM values could be calculated. VBM values were also available from APS measurements, which produced very similar values and trend. The conduction band minimum (CBM) could be calculated by adding the bandgap to the VBM values.

Table S2: *Summary of the Fermi energy (from Kelvin Probe), E-Ef (from XPS), and the VBM (from XPS and APS) values in silicon-tin nanocrystals.*

Diameter of Si-Sn NCs (nm)	Bandgap (eV)		E_f (eV)	E- E_f (eV)	VBM (eV)	
	Tauc plots	SPS			XPS	APS
1.4	1.60	1.65	-4.95	0.54	-5.49	-5.84
1.7	1.80	1.82	-4.92	0.73	-5.65	-5.89
2.2	2.38	1.93	-5.16	0.88	-6.04	-5.94

Figure S20 shows the combined effects of quantum confinement and cluster-doping on the energy band structure of Si-Sn NCs. As can be seen in the Figure S20, the VBM is lowered (on energy scale relative to vacuum) as the size of Si-Sn NCs is increased along with the reduction in the concentration of Sn in Si. The bandgap of Si-Sn NCs is dependent on both the size and the concentration of Sn in Si. As the size of Si-Sn increases, the concentration of Sn decreases thereby increasing the bandgap of Si-Sn NCs. Whereas in case of Si or Sn, the bandgap is entirely dependent on quantum confinement. For instance, the bandgap for Si NCs is increased to around 1.9 eV when the size is reduced to 2 nm.[9]

Similarly, the bandgap for Sn NCs increases from 0.44 eV to 1.24 eV when their size is reduced from 3.5 nm to 2.3 nm.[10] An experimental value for Sn NCs for 1.6 nm is estimated to be around 2.3 eV.[11] The CBM, calculated by adding the bandgap value to the VBM deduced from XPS, also shows an overall reduction trend as the size of Si-Sn NCs is reduced. The Fermi level position moved towards CBM for smaller NCs. The overall changes in the band energy diagram are therefore because of the mutual contributions from both the quantum confinement and cluster doping in Si-Sn NCs, however with the latter exhibiting a stronger influence for smaller NCs.

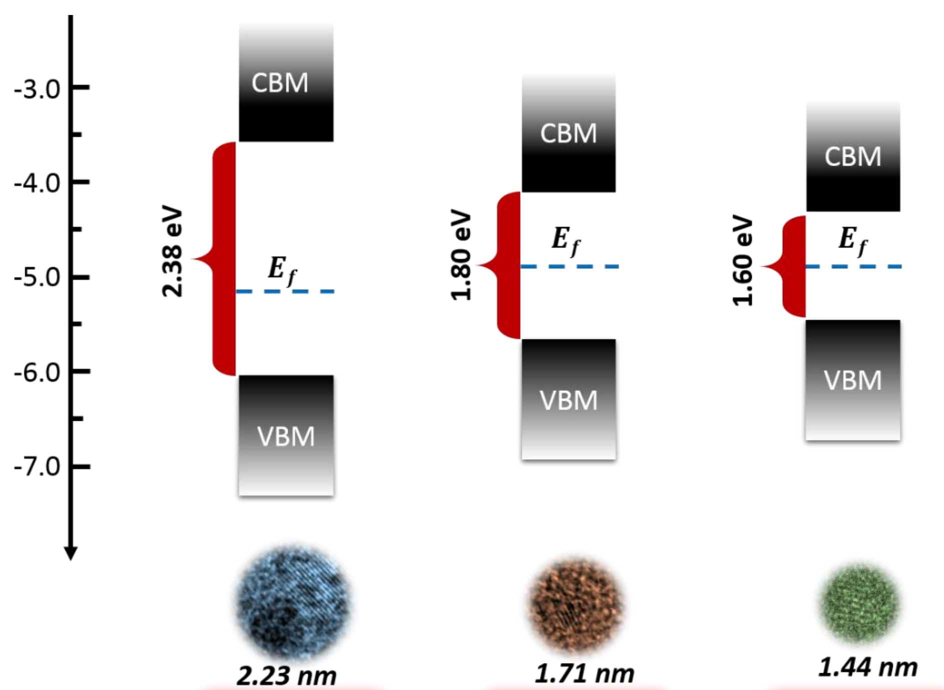

Figure S20: *The energy band diagram of Si-Sn NCs of 1.4 nm, 1.7 nm and 2.2 nm depicting variations in bandgaps and band-edges resulted due to mutual contributions from alloying and quantum confinement. In this diagram we have used bandgap values from Tauc plots and VBM values from the combination of XPS valence band and the Fermi level.*

SI-D. Number of atoms per NC

The number of Sn atoms corresponding to the concentration determined by XPS can be calculated by resolving the following equations for the volume occupied by the Sn cluster (V_{Sn}) and the number of Sn atoms (N_{Sn}):

$$N_{Si} = \rho_{Si} \frac{V - V_{Sn}}{M_{Si}}$$

$$N_{Sn} = \rho_{Sn} \frac{V_{Sn}}{M_{Sn}}$$

$$C_{Sn} = \frac{N_{Sn}}{N_{Si} + N_{Sn}}$$

where N_{Si} is the number of Si atoms in the nanoparticle, $\rho_{Si/Sn}$ is the Si/Sn mass density, V is the total volume of the nanoparticle, $M_{Si/Sn}$ is the mass of the Si/Sn atom and C_{Sn} is the atomic concentration (0 to 1) obtained from XPS measurements (Figure S21). In the calculations we have used amu of Si and Sn to be 28.085 and 118.71 respectively and converted in mass by multiplying by $1.6605390666 \times 10^{-27}$. A density of 2.329 g cm^{-3} and 7.31 g cm^{-3} was used for Si and Sn respectively.

The calculations produce a number of 2.9, 2.5 and 3.5 Sn atoms for the corresponding diameter of 1.4 nm, 1.7 nm and 2.2 nm.

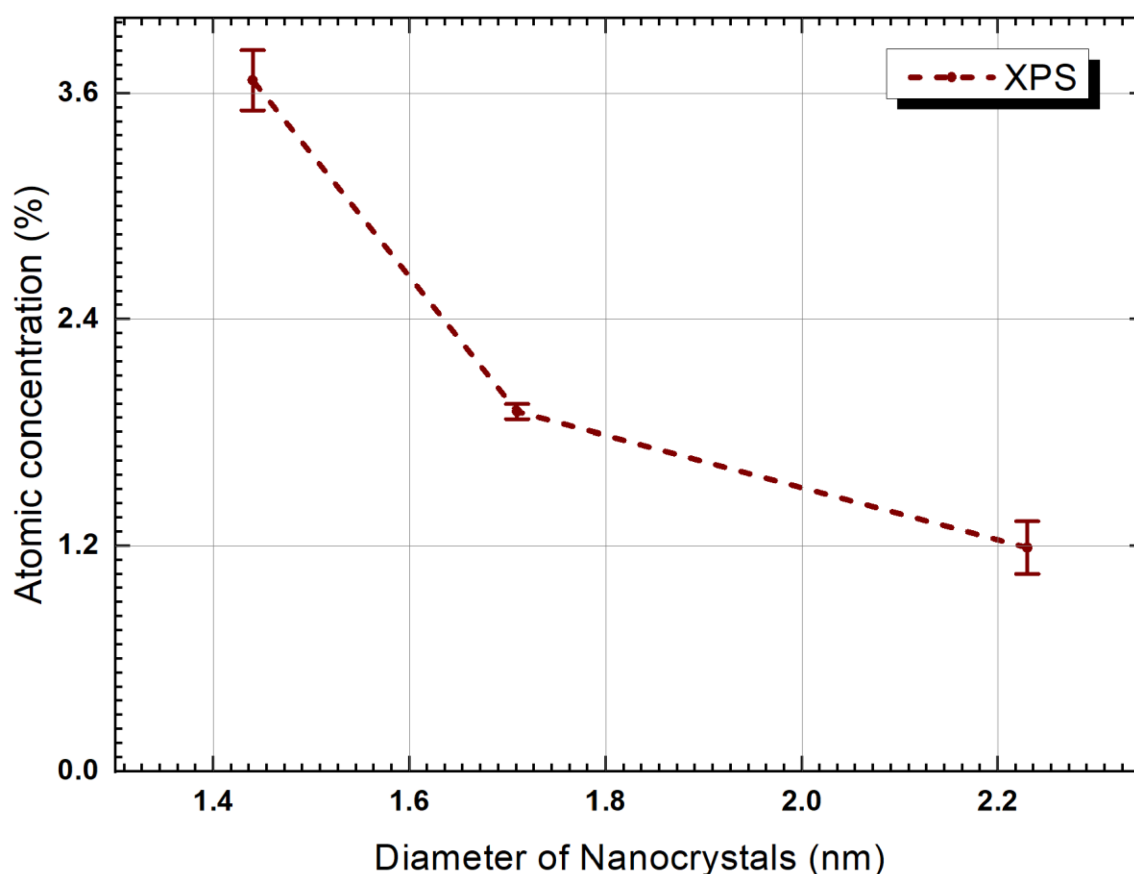

Figure S21: *Variation in atomic concentrations of Sn in Si-Sn NCs along with increasing the size of the NCs. The error bars correspond to the standard deviation from the mean value of three different measurements from each sample.*

SI-E. First-principles calculations

The electronic structure of the optimized NCs is obtained within density functional theory (DFT), as implemented in the first-principles package Turbomole [18], whereby the calculations are performed using the SCAN0 hybrid functional [16, 19], employing the def2-SV(P) [20] and the respective Coulomb fitting basis [21]. The exact exchange contribution is calculated semi-numerically [22, 23]. The total energies were converged with a precision of 10^{-7} a.u.

SI-F. Experimental Details

Plasma reactor setup

Our plasma reactor setup consists of two copper electrodes separated by 2 mm spacing and with aligned holes where a quartz capillary (1 mm external diameter and 0.7 mm internal diameter) is inserted (Figure S22). The plasma is sustained within the quartz capillary and between the copper electrodes. A tin (Sn) wire with a diameter of 0.25 mm was suspended inside the capillary and with one end reaching in between the two electrodes. The Sn wire is used as the sacrificial Sn precursor. Radio-frequency (RF) power of 40 W at 13.56 MHz was applied through a matching unit to one of the electrodes while the other electrode was grounded (figure S22). A digital photograph of the plasma reactor in operation is also shown in Figure S22. Helium gas (1000 sccm constant flow) was used as the background gas for sustaining the plasma between the electrodes. Silane gas was used as silicon (Si) precursor diluted in argon (1% silane in argon) and the corresponding flow was varied and optimized (15 sccm, 25 sccm and 50 sccm) resulting in three different nanocrystal (NC) size distributions. Hydrogen gas also diluted in argon (2% hydrogen in argon, 200 sccm total flow) was also added to the gas mixture. This resulted in an overall composition with He (82% to 80%), Ar (17% to 20%), H_2 (0.33% to 0.32%) and SiH_4 (0.01% to 0.04%).

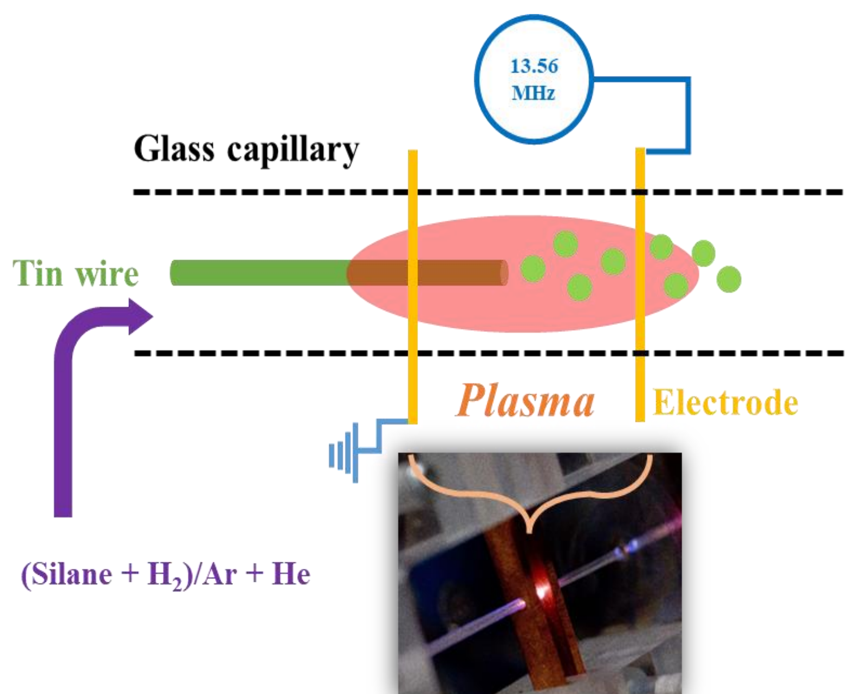

Figure S22: *A schematic diagram and a digital photograph of our plasma reactor configuration at atmospheric pressures that is used to synthesize silicon-tin (Si-Sn) nanocrystals (NCs).*

Material characterization.

Chemical analysis of Si-Sn NCs was performed by Fourier transform infrared spectroscopy (FTIR) and X-ray photoelectron spectroscopy (XPS), the first with a Nicolet iS5 (equipped with an ATR iD5) and the second with an Axis Ultra DLD XPS spectrometer with monochromatic Al Kα X-rays source.

The samples for FTIR and XPS were prepared by directly depositing Si-Sn NCs on Mo substrates and within one day from synthesis. The XPS spectra were collected at a resolution of 0.05 eV and pass energy of 40 eV operating at 10^{-9} bar. The C 1s peak at 284.5 eV was taken for calibrating the spectra. The percent concentration of Sn was determined from XPS survey scan and CasaXPS was used for analysis. Sn 4d and Si 2p were used to estimate their concentration from three different spots. CasaXPS automatically takes into account for the relative sensitivity factors (RSFs). The RSF for Si 2p and Sn 4d were 0.817 and 2.7, respectively as provided by the supplier. Transmission electron microscopy was used to take low and high-resolution images of Si-Sn NCs (JEOL-JEM-2100F electron microscope operated at 200 kV). The samples for TEM measurements were prepared by directly depositing Si-Sn NCs in ethanol from the plasma and immediately drop-casting the colloid (a few drops) onto a TEM grid. The size distribution analysis of the TEM images was performed using ImageJ and the distribution is then represented by a log-normal fit. The analysis of the average spacing of the lattice fringes of the Si-Sn NCs in the HR-TEM images was performed by taking the linear profile of the fringes in Gatan Digital Micrograph software. Ultraviolet-visible spectroscopy (UV-VIS) was performed to extract the transmittance and scattering components from the spectra of Si-Sn NCs. The samples for UV-Vis were prepared by directly depositing onto quartz slides. The relative absorption coefficient was then used to extract the optical bandgap values using Tauc plots. The samples for Fermi level and APS/SPS measurements were prepared on aluminum substrates and the measurement was performed within 1 h.

References

[1] H. Li, M. T. Lusk, R. T. Collins, Z. Wu, *ACS Nano* **2012**, *6*, 9690.
[2] R. H. Fowler, *Phys. Rev.* **1931**, *38*, 45.
[3] M. Lozac'h, V. Švrček, S. Askari, D. Mariotti, N. Ohashi, T. Koganezawa, T. Miyadera, K. Matsubara, *Mater. Today Energy* **2018**, *7*, 87.
[4] J. Tolle, A. V. G. Chizmeshya, Y.-Y. Fang, J. Kouvetakis, V. R. D'Costa, C.-W. Hu, J. Menéndez, I. S. T. Tsong, *Appl. Phys. Lett.* **2006**, *89*, 231924.
[5] P. Moontragoon, Z. Ikonić, P. Harrison, *Semicond. Sci. Technol.* **2007**, *22*, 742.
[6] R. A. Soref, C. H. Perry, *J. Appl. Phys.* **1991**, *69*, 539.
[7] X. Zhang, S. Wen, C. Zhao, H. Zhang, *Mater. Today Commun.* **2021**, *28*, 102543.
[8] J. Tolle, a. V. G. Chizmeshya, Y.-Y. Fang, J. Kouvetakis, V. R. D'Costa, C.-W. Hu, J. Menéndez, I. S. T. Tsong, *Appl. Phys. Lett.* **2006**, *89*, 231924.
[9] M. Macias-Montero, S. Askari, S. Mitra, C. Rocks, C. Ni, V. Svrcek, P. A. Connor, P. Maguire, J. T. S. Irvine, D. Mariotti, *Nanoscale* **2016**, 6623.
[10] G. Allan, C. Delerue, *ACS Nano* **2011**, *5*, 7318.
[11] A. U. Haq, S. Askari, A. Mclister, S. Rawlinson, J. Davis, S. Chakrabarti, V. Svrcek, P. Maguire, P. Papakonstantinou, D. Mariotti, **n.d.**, DOI 10.1038/s41467-019-08661-9.